VACANCY DEFECTS AND MONOPOLE DYNAMICS IN OXYGEN-DEFICIENT PYROCHLORES

A. Diffuse Scattering Program

The diffuse scattering program models the ions as point like particles connected by springs to simulate the lattice dynamics and mimic the Coulomb interaction at low temperatures. This model is commonly called "balls and springs". All the atoms in the system are identified by the three crystallographic coordinates, by the occupancy values (0 for vacancies or 1 in the other case) and by the charge. These ions are then connected only to their closest neighbours using springs of constant F_α, where the index α identifies the bond type between atom pairs. As a first approximation one can choose the springs by looking at the structure of the system [1, 2], and then by comparing the calculated diffuse scattering with the experimental data. The equilibrium length of each spring is chosen to match the stoichiometric lattice parameters. We first put springs between every atom in the lattice, and then proceeded to remove some of them in an ad hoc manner to improve the agreement between the calculated and experimental structural diffuse scattering (for the oxygen-depleted sample). The best arrangement we could find uses a total of 5 spring types that connect Y-O(2), Y-O(1), Ti-O(2), O(2)-O(2) along the longest octahedroid side and O(2)-O(1) along the longest cuboid side as shown in Fig. 1.

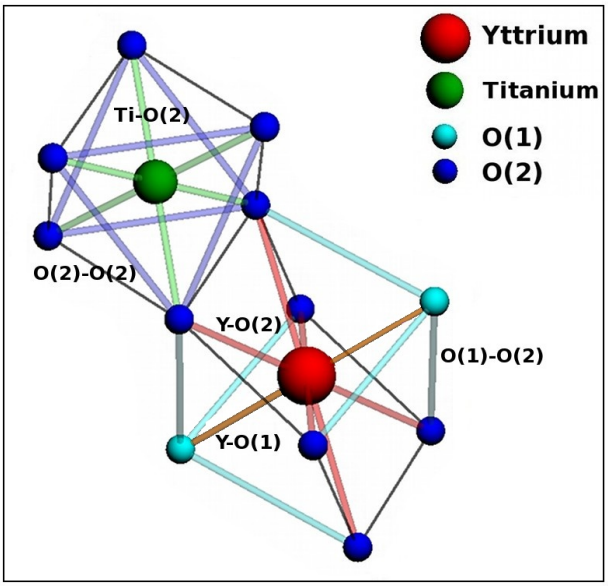

Chemical Bond	Bond Type Index α	Spring Color
Y-O(2)	1	Red
Y-O(1)	2	Orange
Ti-O(2)	3	Green
O(2)-O(2)	4	Blue
O(2)-O(1)	5	Cyan

FIG. 1. *Different springs used in the simulation:* We used a total of 5 types of springs in the system (coloured rods): Y-O(2), Y-O(1), Ti-O(2), O(2)-O(2) along the longest octahedroid side and O(2)-O(1) along the longest cuboid side. The colour of the rods identifies the specific spring type (see adjacent table). Black lines show the cubic and octahedral cages surrounding Y and Ti ions respectively.

In the first stage of the program a model crystal comprising of $64 \times 64 \times 64$ unit cells is generated from the average structure obtained by the refinement of the SXD data with periodic boundary conditions. For each atom the program creates an array containing the coordinates of its nearest neighbours labelled with the appropriate bond index α, then a Marsaglia random generator code is used to remove randomly some O(1) ions according to the depletion value δ, and to create a pair of Ti^{3+} to preserve charge neutrality. Specifically, for every single O(1) removed the program selects randomly two Ti^{4+} among the 12 neighbours of the vacancy, and it changes their charges. This choice is motivated by the fact that the Coulomb energy favours the two Ti^{3+} ions to sit near the oppositely charged vacancy. Other choices are possible but the differences are minimal and discriminating between them is beyond the scope of the present article.

The program assigns to the vacancy a null form factor, so that a vacancy does not contribute either to the crystallographic structure factor or to the intensity of the Bragg peaks when the diffuse scattering is calculated. The possibility of introducing correlations between the positions of the vacancies is discussed in Sec. B.

In order to account for the presence of vacancies in the spring model, we adjust some of the equilibrium spring lengths according to where we expect the effect to be largest on the grounds of energy considerations. (Note that the removal of the springs connecting to a vacancy would be a rather uncontrolled approximation and may lead to lattice instabilities.) These adjustments are commonly called 'size effects' [1, 2]. Here we consider size effects on Yttrium ions when there is only one vacancy nearby and size effects on O(2) ions close to a Ti^{3+}. Note that Y ions between two occasionally close-by vacancies are not expected to displace significantly from their stoichiometric positions because they occupy a symmetric position; therefore, we displace exclusively Y ions close to only one vacancy. The Y ions are moved along the local $\langle 111 \rangle$ directions according to

the symmetry of the system, away from a vacancy as expected from Coulomb interactions (in accord with refs. 3–5), and the value of the shift is set by preliminary comparison with the experimental data. The O(2) anions are moved away from Ti^{3+} towards Ti^{4+} again as expected from Coulomb interactions; the shift is set in order to obtain an average bond length between Ti^{3+}-O(2) $\simeq 2.03$Å as measured in ref. 6, preserving at the same time the average structure of the system (see Fig. 2(c)).

The program attempts then to relax the lattice in response to the size effects, and accounts for thermal fluctuations using a Monte Carlo algorithm. Each ion in the lattice is moved by a random vector drawn from a Gaussian distribution with zero average and standard deviation given by the refinement of the data. Then the Hook energy of the system is computed and the displacements are accepted or rejected according to the usual Metropolis algorithm.

After each Monte Carlo cycle the force constants of the springs are adjusted to obtain the target B_{iso} value of the Titanium ions, which is chosen as reference since the Ti displacements are negligible compared to the other ions. The ratios between the springs are not known a priori, however to a first approximation one can set them by preliminary comparison with the experimental data averaged over the disorder. Monte Carlo cycles are repeated until a sufficiently good convergence is found in the values of the spring constants. Once this is achieved, the spring constants are then fixed and the Monte Carlo simulations are used to compute average quantities of interest, such as the average positions of the ions and the neutron scattering data presented in the manuscript (after averaging over disorder).

We conclude this section explaining the physical origin of the exotic features in the experimental diffuse scattering pattern. We find that the displacement of the Y ions next to a single vacancy is responsible alone for the cross-like pattern at the centre of the (hk7) plane. The four arcs around it are instead due to the relaxation of the other ions. In particular, the size effect introduced on the O(2) ions sitting between Ti^{4+} and Ti^{3+} ions is needed to reproduce the gap in the arcs visible along the axial directions of the plane. Electron density maps were calculated from the x-ray diffraction data using the charge-flipping algorithm in the JANA2006 refinement package [7]. The results presented in Fig. 3 show that the Y ions are displaced along $\langle 111 \rangle$ directions, providing independent confirmation of the defect structure proposed in Fig. 1(a) of the main article.

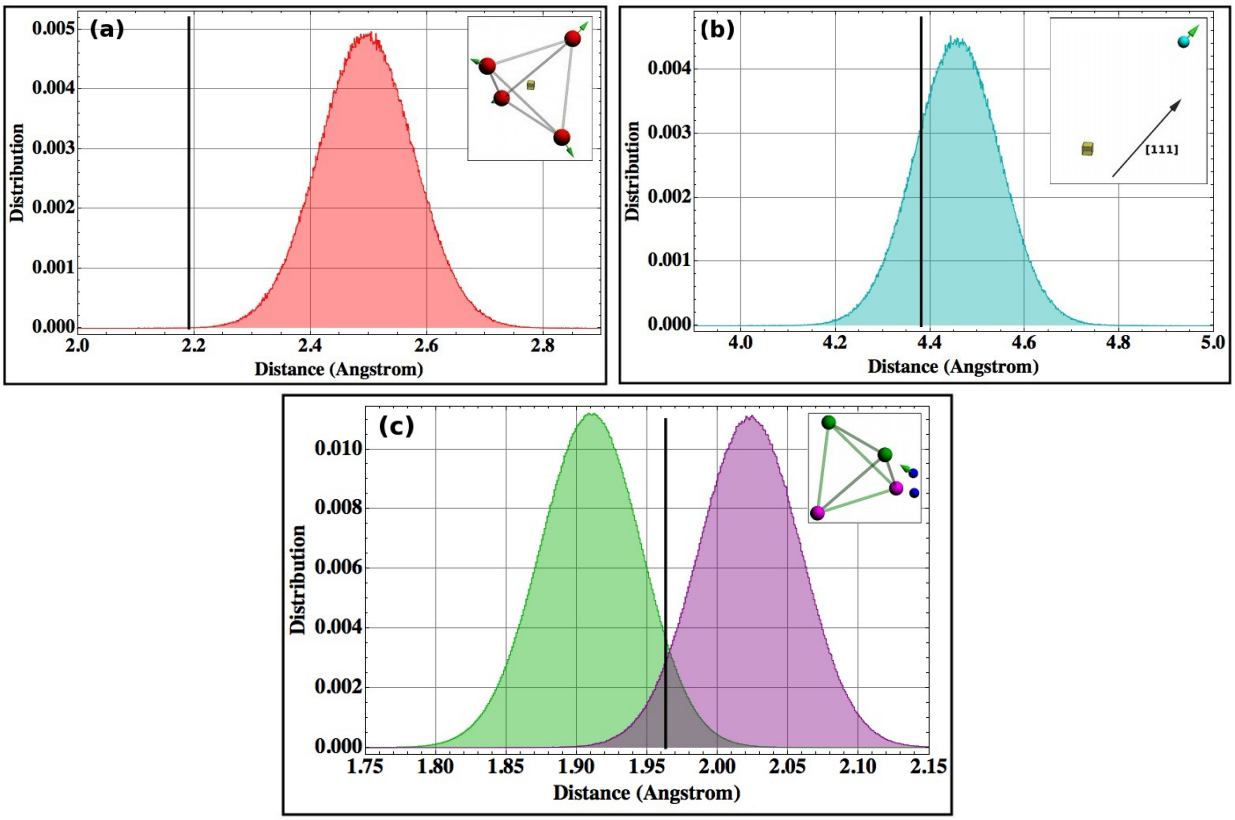

FIG. 2. *Normalised distribution of the distances between the ions:* **(a)** Yttrium-vacancy distance. Yttrium ions are moved away from the vacancy along the local $\langle 111 \rangle$ direction due to the Coulomb repulsion between the cations. **(b)** O(1)-vacancy distance. The O(1) moves away from the vacancy pushed by the shift of the Yttrium. **(c)** $Ti^{4+} - O(2)$ (green) and $Ti^{3+} - O(2)$ (purple) distance. The charge difference of these ions changes the bond lengths with the O(2) ions that move towards the Ti^{4+}. The black line in each panel shows the equilibrium distance in an ideal stoichiometric sample.

The diffuse scattering pattern has been calculated also in other planes for further comparison. Figure 4 shows the experimental (upper half) and calculated (bottom half) diffuse scattering in the (hk8) and (hk11) planes. In all of them we find good agreement

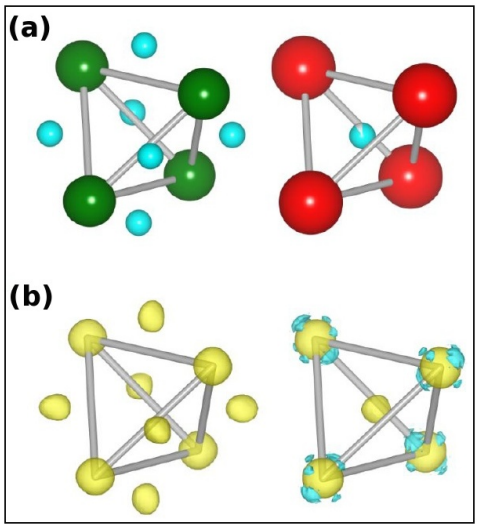

FIG. 3. *Fourier map:* **(a)** Titanium tetrahedron (left) with Ti in green and O(2) in blue, and Yttrium tetrahedron (right) with Y in red and O(1) in blue. **(b)** Electron density map, clearly showing Y displacements along $\langle 111 \rangle$ directions.

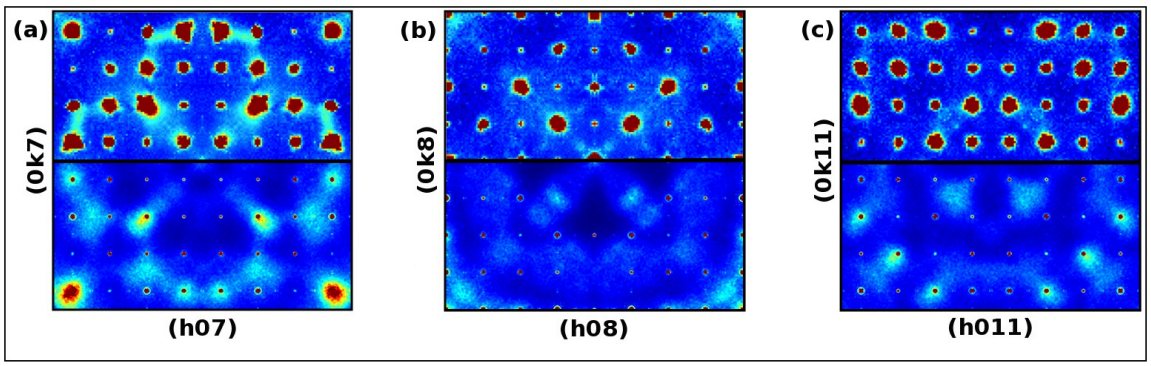

FIG. 4. *Comparison of the experimental diffuse scattering with the Monte Carlo calculation:* The experimental diffuse scattering pattern (upper half quadrant) and the Monte Carlo calculation (bottom half) for **(a)** the (hk7), **(b)** the (hk8) and **(c)** the (hk11) plane. All the exotic features of these planes are very well captured by our Monte Carlo calculation. Notice that all these patterns are calculated using exactly the same values of the parameters we used for the (hk7) plane that was taken as our reference.

between the data and the simulation. Notice that all these patterns have been calculated using exactly the same values of the parameters and spring constants obtained for the (hk7) plane, without additional fitting or adjustments.

Finally in order to complete our analysis, we calculated the diffuse scattering pattern in the (hk7) plane using other models. Firstly, we removed O(2) ions randomly from the lattice according to the depletion value, and we added a size effect on Ti ions, that move away from the vacancy. Secondly, we randomly removed O(1) ions assuming stuffed Y ions on Ti sites to preserve charge neutrality, adding the previous size effects on both Y ions close to the vacancy and on the O(2) close to a stuffed Y^{3+}. Figure 5 shows the experimental (upper half) and calculated (bottom half) diffuse scattering for these models. For O(2) vacancies it is not possible to reproduce the cross at the centre of the plane. If it is assumed that the stuffed compound has O(1) vacancies, the model is essentially the same as Fig. 1(a) of the main article, but with Ti^{3+} ions replaced by Y^{3+} ions, and the diffuse scattering is rather similar. However, the very different scattering lengths of Y to Ti gives some scattering features that are not observed in the data.

B. Correlations between Vacancies

The analysis of the diffuse scattering also provides information about how vacancies are distributed in the system. In order to decide which model to use in the Monte Carlo simulations, we ran some preliminary tests to understand whether the vacancies are distributed at random or their positions appear to be correlated (see Fig. 6). For this stage of the analysis, we used the balls

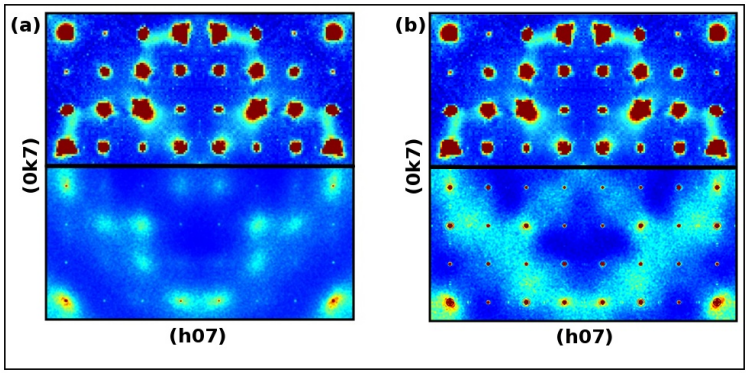

FIG. 5. *Diffuse scattering calculation in the (hk7) plane:* **(a)** O(2) vacancy model, **(b)** O(1) vacancy model plus stuffed Y ions on Ti sites. The first model does not reproduce the cross at the centre of the plane, while the second model shows additional diffuse scattering contributions that are not present in the experimental pattern.

and springs model with only Y size effects. As a result, the gaps in the arcs are not present in the scattering patterns, cf. Fig. 4(a) with Fig. 6(a), right panel.

We compared the case of uniformly distributed vacancies both to the case of positive correlations (favouring clustering of vacancies) and negative correlations (keeping the vacancies apart from one another). The corresponding probability distributions were obtained with a pre-existing algorithm [8, 9] that rearranges the positions of the vacancies starting from a uniform distribution (thus keeping the density constant), until the target degree of correlation is achieved.

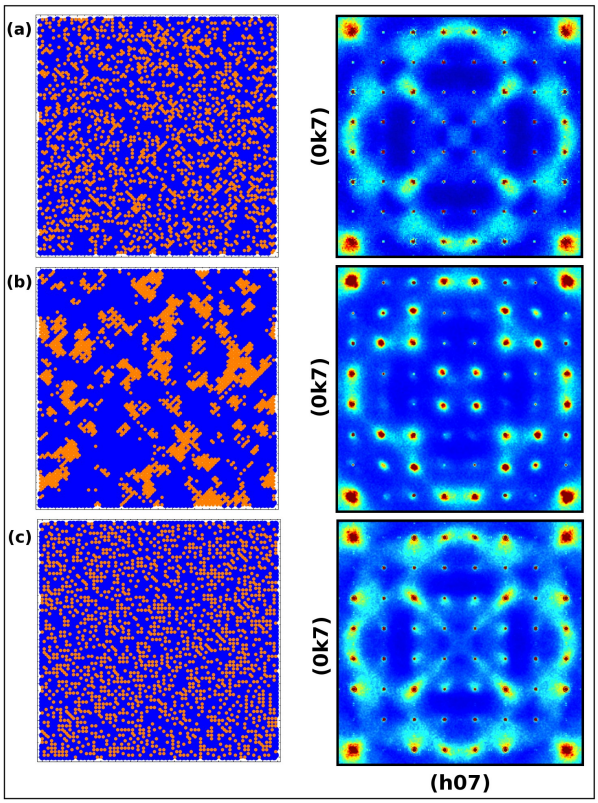

FIG. 6. *Diffuse scattering calculation due to different correlations between vacancies in the system:* **(a)** Randomly distributed, **(b)** positively correlated and **(c)** negatively correlated vacancies. The left panels show a 2D projection of the 3D system (blue) highlighting the positions of the missing Oxygens (orange). For each case we calculated the diffuse scattering pattern (right panels), to be compared with the experimental data in Fig.1 of the main article. The best agreement is clearly given by the choice of a uniformly random distribution.

We can see in Fig. 6 that the random distribution of vacancies gives the best agreement with the experimental diffuse scat-

tering pattern. Positive correlations are unable to reproduce the cross-like pattern at the centre of the plane, whereas negative correlations introduce diffuse scattering intensity features that are not present in the experimental data. For this reason, in the main article we consider only the case of uniformly distributed Oxygen vacancies.

C. Crystal Electric Field Calculation

The analysis of the Crystal Electric Field (CEF) set up by the Oxygen environment surrounding a rare earth ion is key to understand the magnetic properties of spin ice materials. In order to study the effects of Oxygen depletion in these systems, we developed a CEF calculation using the Point Charge Model (PCM) approximation, that approximates the ions as point charges and neglects the overlap between different electron shells. This approximation is generally deemed suitable for rare earth ions (Dy^{3+}) since the *f* orbitals are very well localised.

In order to proceed with the CEF PCM calculations, we used the balls and springs model discussed in the main text to obtain the average positions of the Oxygen ions surrounding a Dy next to a vacancy (averaged over all of the isolated vacancies in the system and over realizations of disorder).

The reference system for the CEF calculation was chosen following Prather's convention, i.e. we put the local [111] easy axis along $\hat{z}$ and one of the C_2 axes along $\hat{y}$ [10]. The following tables show the positions of the ions according to our Monte Carlo calculation averaged over 1000 realisations of disorder, for Dy next to only one (top table) or in between two vacancies (bottom table), in units of the length of the unit cell (approximately 10.12 Å). The reference frame used in the tables is that of the crystallographic unit cell (the specific choice of origin is immaterial since only relative positions are relevant).

Ion Type	x	y	z
Dy	0.6236 ± 0.0167	0.6237 ± 0.0174	0.6241 ± 0.0166
O(1)	0.4950 ± 0.0066	0.4949 ± 0.0073	0.4950 ± 0.0070
O(2)	0.4985 ± 0.0075	0.8016 ± 0.0057	0.4997 ± 0.0079
O(2)	0.7500 ± 0.0073	0.7479 ± 0.0077	0.4501 ± 0.0057
O(2)	0.8014 ± 0.0061	0.4979 ± 0.0076	0.4985 ± 0.0071
O(2)	0.4493 ± 0.0055	0.7491 ± 0.0076	0.7493 ± 0.0070
O(2)	0.4981 ± 0.0070	0.4980 ± 0.0073	0.8020 ± 0.0053
O(2)	0.7496 ± 0.0070	0.4493 ± 0.0055	0.7496 ± 0.0072

Ion Type	x	y	z
Dy	0.6254 ± 0.0080	0.6238 ± 0.0071	0.6256 ± 0.0083
O(2)	0.4975 ± 0.0072	0.7995 ± 0.0052	0.4992 ± 0.0075
O(2)	0.7519 ± 0.0063	0.7512 ± 0.0082	0.4507 ± 0.0060
O(2)	0.8002 ± 0.0050	0.4973 ± 0.0067	0.4978 ± 0.0075
O(2)	0.4513 ± 0.0053	0.7539 ± 0.0076	0.7506 ± 0.0067
O(2)	0.4977 ± 0.0069	0.4966 ± 0.0075	0.7995 ± 0.0057
O(2)	0.7523 ± 0.0073	0.4493 ± 0.0053	0.7529 ± 0.0081

The coordinates of the ions give information on the symmetry of the environment and on the number of Stevens operators needed to describe it. In the case of one vacancy it is still possible to recognise a cube squashed along one main diagonal, even if one of its corners is missing. By contrast when we remove two O(1) we are no longer able to recognise the cubic cage, and the environment has a hexagonal symmetry where the O(2) are alternatingly located above and below the plane of the rare earth ion. In the PCM CEF calculation, the Coulomb potential is approximated by a spherical harmonic expansion. The number of spherical harmonics is directly related to the symmetry of the environment. For the ideal stoichiometric system, the space group is $Fd\bar{3}m$ (D_{3d}), and according to ref. 11 one needs only six Steven's operators in the expansion: $B_{20}, B_{40}, B_{43}, B_{60}, B_{63}$, and B_{66}. The depleted environment where we remove (at least) an O(1) and we relax all the ions in the lattice is far less symmetric. The system has no inversion centre and we are forced to use all 27 Stevens operators. Nevertheless our calculation shows that the six terms in the stoichiometric case are still the dominant ones in the expansion. Indeed the difference in the CEF levels calculated with the full expansion or with an ad hoc expansion truncated to those six terms only is negligible, as illustrated by the following table showing the calculated CEF levels. Notice that all the CEF levels are doublets (d) since Dy^{3+} is a Kramers ion.

Dy^{3+} Level	Full One vacancy (meV)	Reduced One vacancy (meV)	Full Two vacancies (meV)	Reduced Two vacancies (meV)
GS	0.0 (d)	0.0 (d)	0.0 (d)	0.0 (d)
1	14.22 (d)	14.12 (d)	22.11 (d)	21.99 (d)
2	41.35 (d)	41.28 (d)	65.82 (d)	65.73 (d)
3	79.91 (d)	79.85 (d)	131.04 (d)	130.96 (d)
4	126.58 (d)	126.52 (d)	216.57 (d)	216.48 (d)
5	178.48 (d)	178.41 (d)	321.13 (d)	321.05 (d)
6	232.19 (d)	232.12 (d)	442.45 (d)	442.37 (d)
7	285.36 (d)	285.3 (d)	577.44 (d)	577.36 (d)

Figure 7 shows the shape of the anisotropy of the magnetisation calculated in the PCM approximation for a Dy^{3+} ion, applying an external field of 1 Tesla and in the presence of one O(1) vacancy. The large blue spheres are a guide to the eye showing the defective Oxygen environment surrounding the rare earth ion, namely one O(1) (cyan) and six O(2) (blue). The shape of the ellipsoid suggests that the typical strong easy-axis behaviour has been dramatically altered by the vacancy, which produces instead a strong easy plane behaviour perpendicular to the local [111] direction, as is clearly visible in Fig. 7. Figure 8 shows the shape of the anisotropy of the magnetisation for a Dy^{3+} ion between two vacancies. Again, we observe a strong easy plane behaviour. In both cases we find that the magnitude of the in-plane magnetic moment is approximately 5.7 μ_B, reduced with respect to the stoichiometric (easy axis) value 10 μ_B.

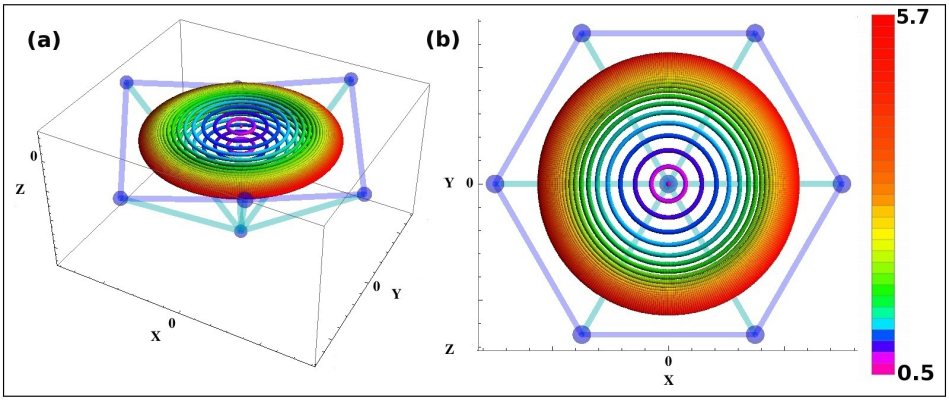

FIG. 7. *CEF calculation of the shape of the anisotropy of the magnetisation in the presence of one vacancy:* **(a)** Each small coloured dot represents the tip of the magnetisation vector centred at the Dy^{3+} ion in response to a given applied external field of 1 Tesla, calculated in the PCM approximation. Many values of the magnetisation are shown simultaneously for applied fields uniformly distributed on the unit sphere. The large spheres show the depleted environment surrounding the rare earth ion: one O(1) (cyan) and and six O(2) (blue). The positions of the atoms were averaged over 1000 realisations of disorder. The ellipsoid shape suggests an easy plane behaviour of the Dy^{3+} in the depleted environment, perpendicular to the local [111] direction. **(b)** Top view of the ellipsoid down the [111] axis. The colour bar indicates the magnitude of the magnetic moment of the rare earth ion in units of Bohr magnetons.

We note that we only considered the surrounding Oxygen ions in constructing the CEF Hamiltonians for the central rare-earth ion, and we ignored the six surrounding Ti ions. The latter are expected to account only for a small correction. In the specific case of Oxygen-depleted samples, some of the surrounding Ti ions are likely Ti^{3+} instead of Ti^{4+}, which could introduce a further (minor) anisotropy in the easy-plane behaviour of a Dy ion close to a vacancy.

D. Monopole Dynamics

A recent comparison between low-temperature magnetic relaxation measurements on spin ice materials and numerical simulations suggests that magnetic impurities acting as monopole pinning centres may be the origin of the surprisingly long time scales observed [12]. It is therefore interesting to see how the magnetic distortion introduced by an O(1) vacancy can act as a pinning centre for the monopoles, thus becoming a prime candidate source of the type of magnetic impurities invoked in ref. 12.

Understanding thoroughly the effects of O(1) vacancies on monopole dynamics is beyond the scope of this article. Here we present a preliminary investigation that illustrates some of the interesting behaviour one may expect to observe.

An Oxygen in position O(1) directly participates in the 4 cages that determine the CEF properties of the 4 neighbouring rare earth ions. In stoichiometric Dy and Ho spin ice, the CEF for each rare earth ion introduces a strong local easy-axis anisotropy. When an O(1) is removed, we have seen in the previous section that the magnetic behaviour of the 4 neighbouring rare earth ions

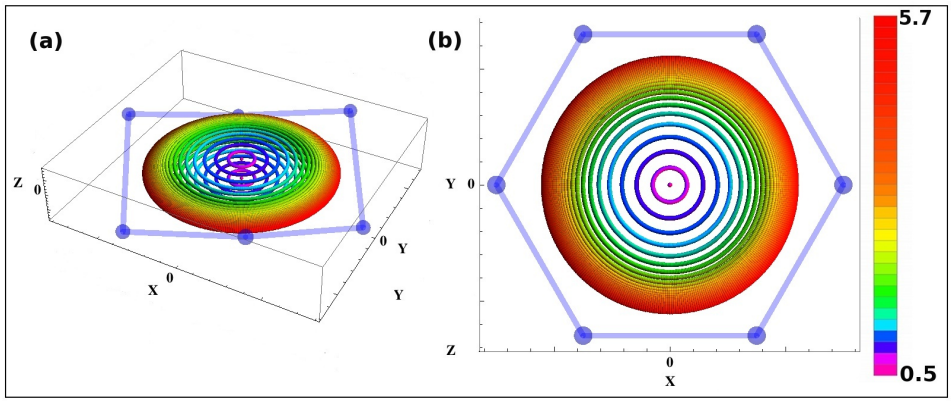

FIG. 8. *CEF calculation of the shape of the anisotropy of the magnetisation in the presence of two vacancies:* **(a)** Same as in Fig. 7, for the case where the Dy ion lies between two vacancies. Again, we find evidence of strong easy-plane behaviour. **(b)** Top view down the [111] axis. Once again the colour bar indicates the magnitude of the magnetic moment in units of Bohr magnetons.

changes dramatically. In the case of Dy^{3+}, which is a Kramers ion, the ground state remains a doublet, the moment is reduced from $10\ \mu_B$ to $5.7\ \mu_B$, and the anisotropy becomes easy plane (perpendicular to the local [111] axis, rather than easy axis (along the local [111] direction). In the case of Ho^{3+} instead, we find that the ground state is a (non magnetic) singlet. In both cases the ground state is separated from excited states by a sizeable energy gap, > 140 K and > 30 K, respectively.

For Dy spin ice, an isolated O(1) vacancy introduces therefore a tetrahedron with 4 easy plane spins surrounded by 4 neighbouring tetrahedra with 3 easy axis and 1 easy plane spin each. We shall refer to this ensemble of spins as a 16-spin cluster. Tetrahedra adjacent to a 16-spin cluster or farther away include a priori only easy axis spins. An example configuration is illustrated in Fig. 9. The case of Ho spin ice is similar, provided that we effectively remove the easy plane spins. The case of

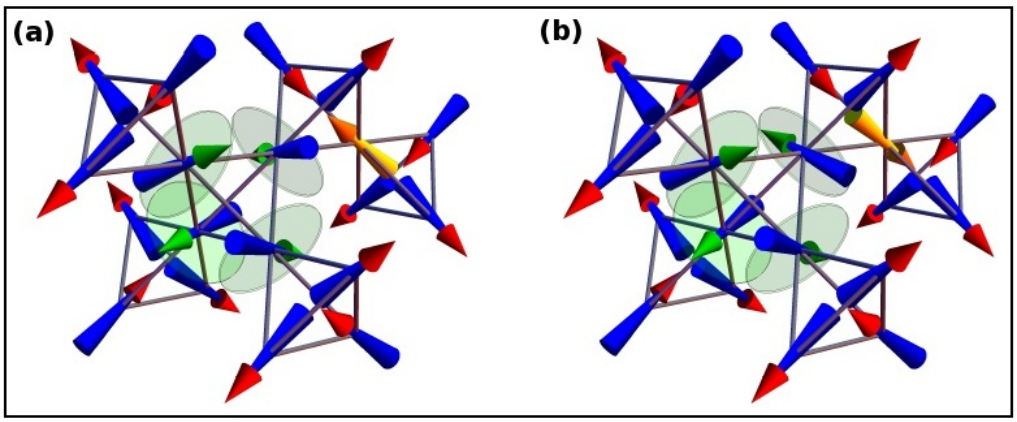

FIG. 9. *Monopole trapping by Oxygen vacancies.* Illustration of the 5 tetrahedra that are directly affected by the change in single-ion behaviour of the 4 Dy ions surrounding an isolated O(1) vacancy (16-spin cluster). An additional tetrahedron is shown adjacent to the cluster, hosting a 3out-1in monopole; the connecting spin is coloured in yellow. Easy-plane spins (green-tip arrows) are free to rotate in the plane perpendicular to the local [111] direction (represented by the corresponding green semi-transparent disc); easy-axis spins (red-tip arrows) can only point directly into or out-of a tetrahedron, as in the stoichiometric case. Given the chosen spin configuration **(a)** and upon flipping the yellow easy-axis spin, the monopole originally sitting in the outlying easy-axis only tetrahedron hops onto one of the 3-easy-axis, 1-easy-plane tetrahedra **(b)**, and it effectively disappears to the eye. In both panels, the direction of the 4 easy-plane spins is chosen to minimise the energy of the system given the orientation of the surrounding easy-axis spins. Notice the small adjustment (most visible in the top right green-tip spin) which is allowed by the continuous easy-plane nature of the spins.

two O(1) vacancies neighbouring one another gives rise to a larger cluster. This is, however, a rare occurrence at low Oxygen depletion and its discussion is beyond the scope of the qualitative arguments presented hereafter, where we focus on isolated vacancies only.

The removal of an O(1) is also likely to affect the superexchange interactions between neighbouring rare-earth ions. These are difficult to estimate from first principles and we shall consider them as free parameters in our qualitative calculations below.

For either $Dy_2Ti_2O_7$ or $Ho_2Ti_2O_7$, the ice rules are no longer well-defined in the 5 tetrahedra closest to a vacancy. When a

monopole (say a 3out-1in defect, as illustrated in Fig. 9) approaches a cluster, it can hop onto the cluster and seemingly disappear. Of course there is no violation of either gauge or magnetic charge conservation in the process: an appropriate measurement of the magnetic flux through a surface surrounding the 16-spin cluster must show that its charge (gauge or magnetic) changes by the appropriate amount. Pictorially, the incoming monopole charge has "delocalised" over 5 tetrahedra and one can no longer identify a specific tetrahedron where it resides.

Whereas at a coarse grained level this may seem immaterial, the process can have measurable consequences on the energy of the system. A significant fraction of the bare cost of a monopole derives from the nearest-neighbour part of the interaction between spins (the energy difference between, say, 3in-1out and 2in-2out on a single tetrahedron). This part of the energy is different for a monopole delocalised over the 5 tetrahedra compared to the case where the monopole sits on a given (stoichiometric) tetrahedron.

This energy difference can be computed explicitly by comparing spin configurations such as those illustrated in Fig. 9. Namely, we compute the change in energy caused by a spin flip process that hops a monopole from a stoichiometric tetrahedron onto one of the 5 tetrahedra affected by the vacancy. Here we limit our considerations to exchange and dipolar interactions truncated at nearest-neighbour distance. Farther range contributions to the energy require large scale Monte Carlo simulations which are beyond the scope of our discussion.

Firstly, we fix the (yellow) spin connecting the outlying (easy-axis) tetrahedron to point in a given direction (immaterial by symmetry), and we impose that the outlying tetrahedron is in a 3out-1in excited state. We then consider all possible configurations of the remaining 11 easy-axis spins in the 16-spin cluster. For each configuration we compute the energy of the system after allowing the easy-plane spins to relax to their ground state. In these calculations we have interactions between easy-axis spins, between easy-plane spins, as well as interactions between easy-axis and easy-plane spins. Since the strengths of the latter two types of interaction are not known a priori, we consider separately the 4 following working assumptions:

1. We naively assume that all the exchange and dipolar coupling constants are the same as in the stoichiometric case.

2. We change the dipolar couplings involving easy-plane spins to account for their reduced magnetic moment of approximately 5.7 Bohr magnetons.

3. We further switch off exchange interactions between easy-plane spins (but not between easy-plane and easy-axis spins). This is the extreme scenario where the removal of an O(1) suppresses the superexchange interaction between Dy spins connected by the missing O(1).

4. Finally, we remove all interactions that involve any of the easy-plane spins. This corresponds to the Ho case where the O(1) vacancy suppresses altogether the magnetic moment of the 4 spins in the central tetrahedron.

In all of the above cases we use the Dy value of the exchange interaction $J/3 = -1.24$ K, with the exception of the last case where we use the Ho value $J/3 = -0.52$ K.

Out of all these 2^{11} configurations, we select a low energy ensemble defined as those configurations whose energy falls within 1 Kelvin of the lowest energy configuration. These are expected to be the relevant configurations at low temperature. For each of them, we flip the yellow spin connecting the 16-spin cluster to the outlying tetrahedron and we compute the corresponding energy difference (after allowing the easy-plane spins to relax to their lowest energy state). This spin flip corresponds to the absorption of a monopole by the 16-spin cluster, and the spin flip energy we compute is the corresponding change in energy of the system. Histograms of the resulting energies from all configurations in the low energy ensemble are shown in Fig. 10, separately for each of the four working assumptions discussed above.

For all four choices of coupling strengths, we observe a broad distribution of energies down to large negative values – large enough to be comparable to the bare energy cost of an isolated monopole (approximately 2.2 K and 3.7 K for Dy and Ho parameters with interactions truncated at the nearest-neighbour level). This means that a monopole coming into contact with a vacancy cluster can become strongly pinned to it. Notice that, given a spin configuration (of the 11 easy-axis spins that we vary), the energy depends on the direction of approach of the monopole.

It is remarkable to notice the similarity in the way that monopoles interact with these Oxygen vacancies compared to the static stuffed moments discussed by Revell *et al*. Depending on the direction of approach, a static magnetic moment can either attract or repel a monopole [12]. Vacancy clusters appear to do just the same, with nearby monopoles being either attracted or repelled depending on the configuration of the 16-spin cluster surrounding a vacancy. Since the static magnetic moments introduced in the simulations by Revell *et al* were able to explain the long-time tail in the magnetic relaxation of the system [12], one can reasonably expect that local magnetic distortions introduced by Oxygen vacancies can lead to similar long-time tails. This is indeed what we see in our experimental results, where the long time tails in the decay of the magnetisation are present in the as-grown sample but disappear upon annealing (see Fig.4 in the main text).

Of course, any distribution of magnetic defects capable of trapping monopoles, and whose pinning energies can be less than the creation of a bare monopole, also alter the thermodynamics of the system. In thermal equilibrium, these magnetic defects act as nucleation centres for monopole defects: it is cheaper to change the configuration of one such magnetic defect and emit a monopole than flipping spins in (locally) stoichiometric spin ice and creating + separating a pair of monopoles. Therefore,

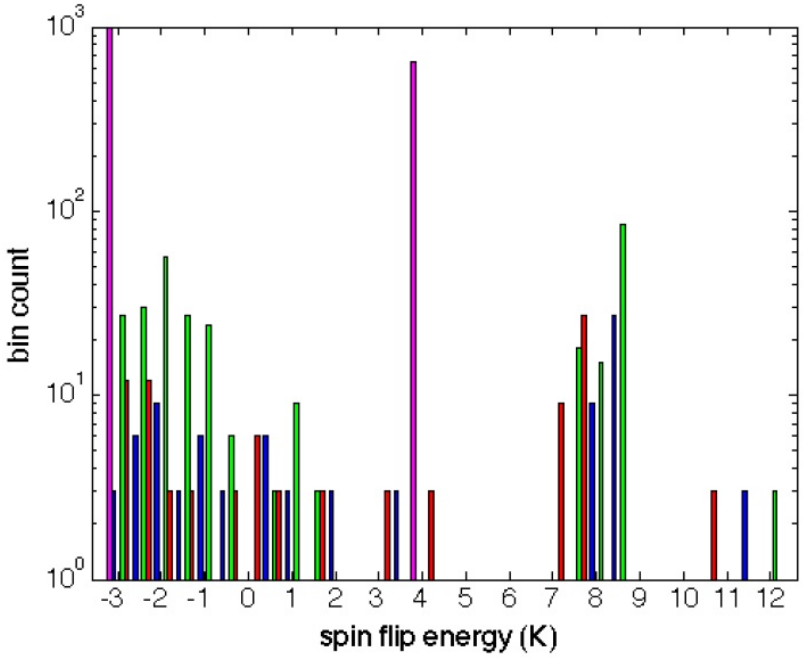

FIG. 10. *Histogram of the energy change for the spin flip process in Fig. 9.* The different colours correspond to different choices of the exchange and dipolar interactions between the spins (truncated at nearest-neighbour distance): In the red histogram, the exchange and dipolar coupling constants are the same as in the stoichiometric case. In the blue histogram, we changed the dipolar couplings involving easy-plane spins to account for their reduced magnetic moment. In the green, histogram we further switched off the exchange interactions between easy-plane spins (but not between easy-plane and easy-axis spins); this is the extreme scenario where the removal of an O(1) vacancy suppresses the exchange interaction between Dy spins connected via the missing O(1). Finally in the magenta histogram, we removed all interactions that involve any of the easy-plane spins; this corresponds to the Ho case where the O(1) vacancy suppresses the magnetic moment of the 4 surrounding spins. In all of the above histograms we used the value of the exchange interaction for Dy, $J/3 = -1.24$ K, with the exception of the last case (magenta) where we used the Ho value, $J/3 = -0.52$ K. [The four distinct histograms have been shifted along the horizontal axis by up to 0.3 K to enhance visibility.]

magnetic defects can raise the monopole density in thermal equilibrium, and correspondingly make the magnetic relaxation dynamics faster [13, 14].

Studying the competition of these two effects, namely the thermodynamic speedup due to increased monopole concentration and the out-of-equilibrium trapping by the very same magnetic defects, is a tall order. A proper understanding of the effect of the trapping energy distribution on the thermodynamic and out-of-equilibrium properties of spin ice requires an extensive study of a many body system that goes well beyond our simple few-body description. Notwithstanding, it is tempting to speculate that the speed-up is more likely to dominate at intermediate time scales, when the system is close to thermodynamic equilibrium, whereas the slowing down due to pinning should become important in the far from equilibrium motion of monopoles. Intriguingly, this (very naive) picture is in fact consistent with our experimental data (Fig.4 in the main text), which shows indeed an initial slowing down of magnetic relaxation in the annealed sample with respect to the as-grown one.

[1] Welberry T. R. et al., The interpretation and analysis of diffuse scattering using Monte Carlo simulation methods. Acta Cryst. A **64**, 23-32 (2008).

[2] Goossens D. J. et al., Monte Carlo modelling of diffuse scattering from single crystals: The program ZMC. Metal. Mater. Trans. A **42**, 23-31 (2011).

[3] Welberry T. R., Diffuse x-ray scattering and models of disorder. IUCr Monographs on Crystallography **16** (OUP, 2004).

[4] Welberry T. R., Single crystal neutron diffuse scattering and Monte Carlo study of the relax or ferroelectric $\mathrm{PbZn_{1/3}Nb_{2/3}O_3}$ (PZN). J. Appl. Cryst **38**, 639-647 (2005).

[5] Gutmann, M. J. Accelerated computation of diffuse scattering patterns and application to magnetic neutron scattering. J. Appl. Cryst. **43**, 250-255 (2010).

[6] Abrahams S. C., Magnetic and crystal structure of titanium sesquioxide Phys. Rev. **130**, 2230-2237 (1963).

[7] Oszlányi, G., Süto, A. Ab initio structure solution by charge flipping. Acta Cryst. A **60**, 134-141 (2004).

[8] Welberry T. R., Diffuse x-ray scattering and models of disorder. Rep. Prog. Phys. **48**, 1543-1593 (1985).
[9] Proffen T., Neder R., "DISCUS 3.4 users guide", www.pa.msu.edu/cmp/billingegroup/discus/dis_man.pdf.
[10] Hutchings M. T., Point-charge calculations of energy levels of magnetic ions in crystalline electric fields. In Seitz, F., Turnbull, D. (Eds.), Solid State Physics **16**, 227-273 (Academic Press, 1964).
[11] Walter U., Treating crystal field parameters in lower than cubic symmetries. J. Phys. Chem. Solids **45**, 401-408 (1984).
[12] Revell H. M. et al., Evidence of impurity and boundary effects on magnetic monopole dynamics in spin ice. Nature Phys. **9**, 34-37 (2013).
[13] Ryzhkin I. A., Magnetic relaxation in rare-earth oxide pyrochlores. J. Exp. Theoret. Phys. **101**, 481-486 (2005).
[14] Jaubert L. D. C., Holdsworth P. C. W., Signature of magnetic monopole and Dirac string dynamics in spin ice. Nature Phys. **5**, 258-261 (2009).